Propeller Thrust and Drag in Forward Flight

Rajan Gill and Raffaello D'Andrea

***Abstract*— This paper presents a methodology for modelling the thrust, drag, and torque of propellers used in unmanned-aerial-vehicle (UAV) applications. The model can be used in wide flight regimes from hover to high speed forward flight and is derived from first-principles using Blade Element Theory (BET), Blade Element Momentum Theory (BEMT), and a parameter fitting procedure to determine aerodynamic parameters. The methodology is applied to three different types of propellers to showcase its versatility, and experiments show that the procedure can accurately predict the rotor forces. Wind tunnel measurements are also included to serve as an additional basis for comparison. A comparison to static thrust models typically used by roboticists is also shown.**

I. INTRODUCTION

In order to analyze aerodynamic properties of an unmanned-aerial-vehicle (UAV), wind tunnel experiments must be performed or system identification can be done from experimental flights. Being able to predict the propeller thrust and rotor drag can help identify other aerodynamic properties of a UAV, such as the drag of the vehicle or the amount of lift a wing produces. An accurate rotor thrust and drag map can also be used for high fidelity simulation models, and for control purposes to improve performance of autonomous UAVs.

The typical approach has been to model the thrust of the propeller to be proportional to the square of its rotation rate and to neglect rotor drag in forward flight [1], [2], [3], [4], [5], [6], [7], [8], [9], [10]. However, as the vehicle flies with some forward velocity, the accuracy of this model deteriorates. This is especially the case in high speed (and high pitch) flight, as will be shown in this paper. Generally it is good to know when this simplified model of rotor forces works well and under what conditions does it detiorate.

The thrust map developed in [11], [12] requires that the mechanical power of each propeller be known. This requires current sensing on each motor which can lead to bulky electronics and requires an accurate electrical to mechanical efficiency model. For some UAVs, current draw information is not available for each individual motor and/or can be riddled with noise [13]. Furthermore, [11], [12] neglect rotor drag and assume uniform induced inflow through the rotor disk. The rotor force maps developed in this paper does not make such assumptions and does not make use of power information.

This work was supported by the Natural Sciences and Engineering Research Council of Canada (NSERC) and the Swiss National Science Foundation (SNSF).

The authors are with the Institute of Dynamic Systems and Control (IDSC) in the Mechanical and Process Engineering Department, ETH Zurich, 8037 Zurich, Switzerland {rgill, rdandrea}@ethz.ch

In [14], [15], [16], blade element theory (BET) is used to model the propeller thrust, however, unlike in this paper, small angle approximations are used for simplicity. Such approximations are valid for larger rotor disks [15] or for UAVs that fly at relatively low speeds, however it was found for our experiments, where the UAVs reach speeds up to 14.5 m/s using a propeller with a radius of 10 cm, the small angle approximations are no longer reasonable. Furthermore, [14], [17] also assume uniform inflow across the rotor disk and neglects rotor drag. In [15], [18], BET is combined with blade element momentum theory (BEMT) to model rotor thrust, but only in axial climb and while also using small-angle approximations (since their applications are intended for large rotor disks on helicopters and wind turbines). In [16] BET and BEMT is combined for UAV applications, but again in axial climb. This model becomes inaccurate during forward flight (control volume changes as the rotor disk has a non-zero angle with the freestream airflow [15, 2.14]; rotor drag becomes existential).

In this paper, BEMT is combined with BET in forward flight, which has not been done before according to the authors' knowledge, to construct a rotor thrust and drag map. A parameter fitting procedure is then done to determine the aerodynamic parameters used in the BET formulation, and requires the UAV to fly levelled flights at various constant speeds. The entire methodology is described in Sections II and III. The technique is then applied in Section IV to two different propellers: one soft propeller meant for hovering vehicles and a stiff propeller meant for forward flying applications, to show the technique can characterize both types of propellers accurately. A comparison is also done of the model to direct load measurements in a wind tunnel for a third propeller. Furthermore, this paper depicts the limitation of the standard static thrust model when used in forward flight; this comparison has not been done before in the literature.

A. Notation

Let $\langle \vec{x}, \vec{y} \rangle$ denote the inner product of vectors $\vec{x}$ and $\vec{y}$ in $\mathbb{R}^n$. The Euclidean norm of a vector $\vec{x}$ is denoted by $x = \|\vec{x}\|$.

II. PROPELLER MODELING

In this section, we derive the rotor average thrust T, drag D, and torque τ given that the propeller rotates at a rate Ω, the rotor disk has velocity $\vec{V}$, and the rotor has a tilt vector $\hat{z}$, see Fig. 1.

The propeller has radius R, with N_b blades per propeller. It is also assumed that the pitch angle and chord length of

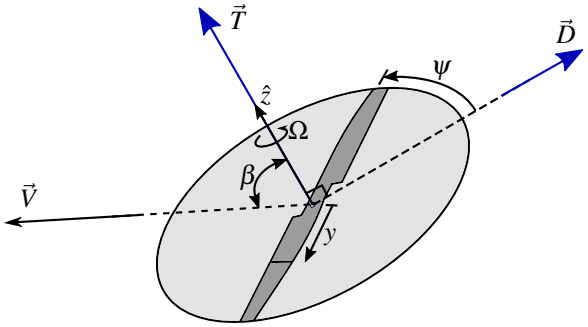

Fig. 1: Rotor disk. Forces shown in blue. The rotor drag vector $\vec{D}$ lies on the rotor disk plane $\hat{z}$ and is aligned with the velocity vector $\vec{V}$.

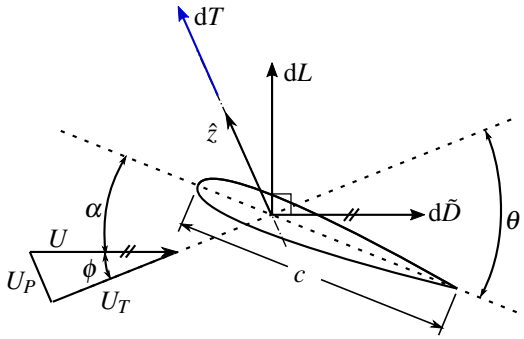

Fig. 2: Forces and angles shown for an infinitesimal blade element located at y from the rotor center (see Fig. 1). The differential drag d$\tilde{D}$ of the blade element acts along $\vec{U}$ and is not the differential rotor drag dD.

the blade is known at any point along the propeller blade, represented by the maps

$$\theta : [0,R] \to [0,\pi/2]$$
$$c : [0,R] \to \mathbb{R}$$

respectively. In practice, these maps can be approximated by spline interpolating measured values along the propeller blade.

To simplify the derivations in the subsequent sections, let

$$\beta := \arccos\left(\frac{\left\langle \vec{V},\ \hat{z}\right\rangle}{V}\right), \qquad V \neq 0$$

be the angle between the freestream velocity and rotor disk plane. The angle ψ represents the azimuth angle of a propeller blade within the rotor disk, where $\psi = 0$ is defined to be the point where the propeller is parallel to the projection of $\vec{V}$ on to the rotor disk plane, i.e. $\text{proj}_{\hat{z}}(\vec{V})$, which is also the direction of the rotor drag (see Fig. 1). Rotor drag occurs only during forward flight, where each blade of the propeller sees a difference in freestream velocity as it completes a revolution, thereby resulting in a net drag. Rotor thrust acts along $\hat{z}$.

A. Blade Element Theory

BET is the process of dividing up a propeller blade into infinitesimal segments or "elements". The quasi-steady aerodynamic forces will be derived for each element of the blade. A function's dependence on Ω, V and β will be dropped for brevity.

Let $y \in [0,R]$ represent the distance of the differential blade segment from the center of the propeller (see Fig. 1), and let the segment have a width of dy. Then, the velocity components of the air seen by the blade in the tangential and perpendicular directions to the rotor disk are

$$U_T(y,\psi) = \Omega y + V\sin(\beta)\sin(\psi) \tag{1}$$
$$U_P(y,\psi) = V\cos(\beta) + v_i(y), \tag{2}$$

respectively, where v_i is the induced inflow velocity through the rotor disk [15], and will be solved for in Section II-C. The angle ϕ is defined (see Fig 2)

$$\phi(y,\psi) := \arctan\left(\frac{U_P(y,\psi)}{U_T(y,\psi)}\right)$$

and the angle of attack of the blade element is then (see Fig. 2)

$$\alpha(y,\psi) = \theta(y) - \phi(y,\psi).$$

When the fluid is in steady state motion, the aerodynamic lift and drag forces of the blade element are defined to be [19]

$$\text{d}L(y,\psi) = \frac{1}{2}\rho U(y,\psi)^2 C_L(\alpha(y,\psi))c(y)\text{d}y$$
$$\text{d}\tilde{D}(y,\psi) = \frac{1}{2}\rho U(y,\psi)^2 C_D(\alpha(y,\psi))c(y)\text{d}y.$$

where $U := \sqrt{U_T^2 + U_P^2}$, ρ is the air density, dL and d$\tilde{D}$ are the aerodynamic force acting perpendicular and tangential to the freestream velocity of the blade element at distance y from the rotor's center. Nonlinear, parametric forms of the normalized lift and drag C_L[1] and C_D are given below [20], [19]

$$C_L(\alpha) = (1-\sigma(\alpha))c_{l,1}\alpha + \sigma(\alpha)c_{l,2}\sin(\alpha)\cos(\alpha) \tag{3}$$
$$C_D(\alpha) = c_d\sin(\alpha)^2 + 2\frac{1.02c_p}{\sqrt{RN(y,U(y,\psi))}} + c_{d,0} \tag{4}$$

where $c_{l,1}$, $c_{l,2}$, c_d are parameters to be empirically determined in Section III, c_p is the skin friction drag coefficient for laminar flow [19, Blasius Theory], $RN(y,U) = \frac{\rho U c(y)}{\mu}$ is the Reynolds number, μ is the air viscosity, $c_{d,0}$ is the form-drag coefficient[2], and $\sigma(\cdot)$ is a sigmoid function given by [20]

$$\sigma(\alpha) = \frac{1 + \text{e}^{-M(\alpha-\alpha_0)} + \text{e}^{M(\alpha+\alpha_0)}}{\left(1+\text{e}^{-M(\alpha-\alpha_0)}\right)\left(1+\text{e}^{M(\alpha+\alpha_0)}\right)}$$

where M, α_0 are parameters[2]. This sigmoid function is used to approximate an airfoil's stall effect and the roll-off in lift

[1] A simplified form of $C_L(\alpha) = c_l\sin(\alpha)\cos(\alpha)$ also works well, reducing the number of airfoil parameters by two and computation time (see Section IV) by an order of magnitude.

[2] Typical values are $\rho = 1.225$ kg/m^3; $c_p = 1.328$ [19]; $\mu = 1.983\text{E}{-5}$ Pa·s; $M = 50$ [20]; $c_{d,0} = 0.01$ [21].

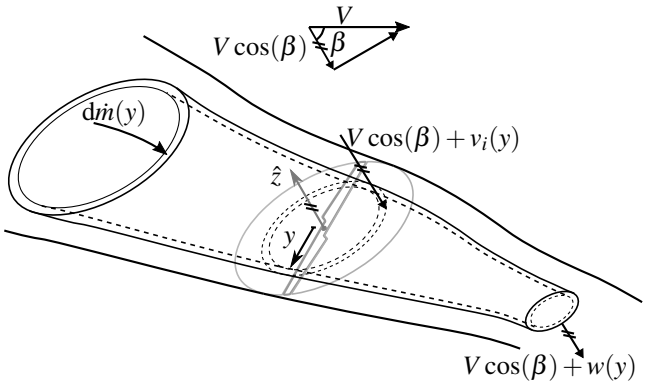

Fig. 3: Infinitesimal control volume located at distance y from the rotor center (see Fig. 1). In this case shown, the wake is behind the rotor disk.

as $\alpha \to \pi/2$. The parameter α_0 will depend on the propeller airfoil and will be empirically determined in Section III. Note that C_D doesn't contain the typical induced drag term from wing-tip vortexes [19], since each blade element doesn't produce vortexes except at the very tip of the propeller blade.

Ultimately we are interested in the forces perpendicular (rotor thrust) and tangential (rotor drag) to the rotor disk irrespective of the propeller azimuth angle ψ, which is done with a rotation and averaging

$$\begin{aligned}\mathrm{d}T_{\mathrm{BET}}(y) = \frac{N_b}{2\pi}\int_0^{2\pi} &(\mathrm{d}L(y,\psi)\cos(\phi(y,\psi)) \\ &-\mathrm{d}\tilde{D}(y,\psi)\sin(\phi(y,\psi)))\,\mathrm{d}\psi \end{aligned} \tag{5}$$

$$\begin{aligned}\mathrm{d}D(y) = \frac{N_b}{2\pi}\int_0^{2\pi} &(\mathrm{d}L(y,\psi)\sin(\phi(y,\psi)) \\ &+\mathrm{d}\tilde{D}(y,\psi)\cos(\phi(y,\psi)))\sin(\psi)\mathrm{d}\psi \end{aligned} \tag{6}$$

where $\mathrm{d}T_{\mathrm{BET}}$, $\mathrm{d}D$ are now the differential rotor thrust and drag, respectively, using the BET formulation. The propeller torque of the differential element can also be computed

$$\begin{aligned}\mathrm{d}\tau(y) = y\frac{N_b}{2\pi}\int_0^{2\pi} &(\mathrm{d}L(y,\psi)\sin(\phi(y,\psi)) \\ &+\mathrm{d}\tilde{D}(y,\psi)\cos(\phi(y,\psi)))\,\mathrm{d}\psi \end{aligned} \tag{7}$$

B. Blade Element Momentum Theory

The induced inflow $v_i(y)$ depends on the propeller geometry $\theta(y)$, $c(y)$ and the operating conditions V, Ω, β. In previous works, $v_i(y)$ is approximated using various empiracle models [15, 3.5.2], or using a uniform inflow model from standard momentum theory [14]. In this section, momentum theory is applied to an infinitesimal rotor disk (see Fig. 3) to assist in the computation of the (not necessary uniform) induced inflow $v_i(y)$ by combining the results with BET in Section II-C. The flow is assumed to be adiabatic, inviscid, and incompressible. To the best of the authors' knowledge, BEMT has not been applied to forward flying applications to derive the inflow.

The differential control volume is shown in Fig. 3. By applying the Glauert mass flow model [15, 2.14] to the differential control volume, the differential mass flow rate is

$$\mathrm{d}\dot{m}(y) = \rho 2\pi y \mathrm{d}y\sqrt{(V\sin(\beta))^2 + (V\cos(\beta)+v_i(y))^2}$$

where as before, $v_i(y)$ is the inflow field and will be solved for in Section II-C.

Applying the conservation of momentum in the thrust direction depends on whether the wake region is above ($V\cos(\beta) > 0$) or below ($V\cos(\beta) < 0$) the rotor disk [15]. The following derivation is shown for the case when the wake is below the rotor disk (Fig. 3). Let $w(y)$ represent the wake flow, then applying momentum theory yields

$$\begin{aligned}\mathrm{d}T_{\mathrm{BEMT}}(y) &= \mathrm{d}\dot{m}(V\cos(\beta)+w(y)) - \mathrm{d}\dot{m}(V\cos(\beta)) \\ &= \mathrm{d}\dot{m}(y)w(y)\end{aligned} \tag{8}$$

When the wake is above the rotor disk, the right-hand side of (8) is negated. If the rotor is in a vortex ring state ($V\cos(\beta) < 0$ and $V\cos(\beta)+v_i > 0$), momentum theory is violated and there is no analytic expression for the induced inflow [15]. This case doesn't occur in the experiments in Section IV, however an approximation one could use is the static induced inflow (12).

Applying the conservation of power,

$$\begin{aligned}&\mathrm{d}T_{\mathrm{BEMT}}(y)(V\cos(\beta)+v_i(y)) \\ &\quad= \frac{1}{2}\mathrm{d}\dot{m}(y)\left(\left((V\cos(\beta)+w(y))^2 + (V\sin(\beta))^2\right) - V^2\right) \\ &\quad= \mathrm{d}\dot{m}(y)(V\cos(\beta)w(y) + \frac{1}{2}w(y)^2).\end{aligned} \tag{9}$$

Combining (8) and (9) yields $w(y) = 2v_i(y)$ and thus

$$\begin{aligned}&\mathrm{d}T_{\mathrm{BEMT}}(y) = 2v_i(y)\mathrm{d}\dot{m}(y) \\ &\quad= 4v_i(y)\rho\pi y\mathrm{d}y\sqrt{(V\sin(\beta))^2 + (V\cos(\beta)+v_i(y))^2}.\end{aligned} \tag{10}$$

C. Hybrid Blade Element Momentum Theory

The only unknown in (5) and (10) is the inflow field $v_i(y)$. The BET and BEMT maps are combined to solve for the inflow velocity field by setting up a root finding problem as follows. First, treat v_i as a variable to the two functions (5) and (10) to yield $\mathrm{d}T_{\mathrm{BET}}(y, v_i)$ and $\mathrm{d}T_{\mathrm{BEMT}}(y, v_i)$. Then, the inflow field $v_i(y)$ can be solved for using the following

$$v_i(y) = \text{find}\, v_i^* \text{ s.t. } \mathrm{d}T_{\mathrm{BET}}(y, v_i^*) = \mathrm{d}T_{\mathrm{BEMT}}(y, v_i^*). \tag{11}$$

In practice, (11) is solved using Python's SciPy package. To hasten the solve time, a smart choice of the initial guess $v_{i0}^*(y)$ should be used. One choice for the initial guess is the uniform inflow at hover, for which a closed form solution is derived for in [15, 2.2.2]

$$v_{i0}^*(y) \equiv \sqrt{\frac{T_{\mathrm{static}}}{2\rho\pi R^2}} \tag{12}$$

where $T_{\mathrm{static}} \propto \Omega^2$ is the static thrust (i.e. when $V = 0$) produced by the propeller.

Now that the field $v_i(y)$ is known[3], it can be used in (2)

[3]For fixed-wing UAVs whose wing is behind the slipstream of the rotor, the induced inflow field $v_i(y)$ can also be used to determine the true angle of attack and freestream velocity seen by the wing.

in the BET formulation to yield the desired averaged rotor thrust, drag, and torque of a blade element. The full rotor thrust can then be determined by integrating with respect to y

$$\begin{aligned} T &= \int_0^R \left(\frac{\mathrm{d}T_{\mathrm{BET}}(y)}{\mathrm{d}y} \right) \mathrm{d}y \qquad (13) \\ &= \int_0^R \left(\frac{N_b}{2\pi} \int_0^{2\pi} \frac{1}{2} \rho U(y,\psi)^2 c(y) (C_L(\alpha(y,\psi)) \cos(\phi(y,\psi)) \right. \\ &\qquad \left. - C_D(\alpha(y,\psi)) \sin(\phi(y,\psi))) \mathrm{d}\psi \right) \mathrm{d}y \end{aligned}$$

and similarly for the rotor drag

$$\begin{aligned} D &= \int_0^R \left(\frac{\mathrm{d}D(y)}{\mathrm{d}y} \right) \mathrm{d}y \qquad (14) \\ &= \int_0^R \left(\frac{N_b}{2\pi} \int_0^{2\pi} \frac{1}{2} \rho U(y,\psi)^2 c(y) (C_L(\alpha(y,\psi)) \sin(\phi(y,\psi)) \right. \\ &\qquad \left. + C_D(\alpha(y,\psi)) \cos(\phi(y,\psi))) \sin(\psi) \mathrm{d}\psi \right) \mathrm{d}y. \end{aligned}$$

The propeller torque can also be computed by integrating (7)

$$\begin{aligned} \tau &= \int_0^R \left(\frac{\mathrm{d}\tau(y)}{\mathrm{d}y} \right) \mathrm{d}y \qquad (15) \\ &= \int_0^R \left(y \frac{N_b}{2\pi} \int_0^{2\pi} \frac{1}{2} \rho U(y,\psi)^2 c(y) (C_L(\alpha(y,\psi)) \sin(\phi(y,\psi)) \right. \\ &\qquad \left. + C_D(\alpha(y,\psi)) \cos(\phi(y,\psi))) \mathrm{d}\psi \right) \mathrm{d}y. \end{aligned}$$

III. PARAMETER IDENTIFICATION

The aerodynamic parameters to identify in the rotor thrust and drag maps (13)-(15) are $x := (c_{l,1}, c_{l,2}, c_d, \alpha_0)$. In this section, an experiment and algorithm is designed to identify the parameter vector x. First, bring back the rotor force maps (13)-(15) dependence on Ω, β, V and with a slight abuse of notation, parametrize them by x, to yield the maps $T(\Omega,\beta,V,x)$ and $D(\Omega,\beta,V,x)$.

Let the UAV have n rotors, each producing a thrust and drag of $T_i := T(\Omega_i,\beta_i,V_i,x)$, $D_i := D(\Omega_i,\beta_i,V_i,x)$, $i \in \{1,\dots,n\}$, respectively, where the subscript i denotes the i'th rotor. The vehicle flies with velocity $\vec{V}_{\text{vehicle}}$ with body rate $\vec{\omega}$, and let $\vec{r}_i$ be the vector from the vehicle's center to the location of rotor disk i. Then, in general, each rotor disk has a velocity of

$$\vec{V}_i = \vec{V}_{\text{vehicle}} + \vec{\omega} \times \vec{r}_i$$

and thus $\beta_i = \arccos\left(\left\langle \vec{V}_i, \hat{z}_i \right\rangle / V_i \right)$ as before.

The UAV is then commanded to perform levelled flights at various constant speeds V_{vehicle}. Assuming the vehicle is a multirotor[4], at steady state the vertical forces (see Fig. 4) are balanced

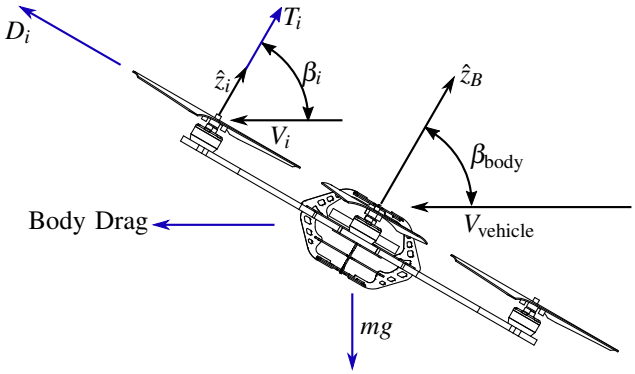

Fig. 4: Planar view of the vehicle with forces shown in blue. Each rotor produces a thrust T_i and drag D_i, for $i \in \{1,\dots,n\}$. The vector $\hat{z}_B$ is the plane of the multirotor frame.

$$\sum_{i=1}^n T(\Omega_i,\beta_i,V_i,x) \sin(\beta_i) + \sum_{i=1}^n D(\Omega_i,\beta_i,V_i,x) \cos(\beta_i) = mg \qquad (16)$$

where m is the mass of vehicle and g is the acceleration due to gravity. By flying at N various operating conditions $\Omega_{(i,j)}, \beta_{(i,j)}, V_{(i,j)}, V_{(\text{vehicle},j)}$, for $j = 1,\dots,N$, (16) can be used to identify the aerodynamic parameter vector x in a least squares sense as follows: first define the error vector

$$\begin{aligned} \vec{\varepsilon}(x)_j := &\sum_{i=1}^n T(\Omega_{(i,j)},\beta_{(i,j)},V_{(i,j)},x) \sin(\beta_{(i,j)}) + \\ &\sum_{i=1}^n D(\Omega_{(i,j)},\beta_{(i,j)},V_{(i,j)},x) \cos(\beta_{(i,j)}) - mg, \qquad (17) \end{aligned}$$

for $j = 1,\dots,N$, where $\vec{\varepsilon}(x) \in \mathbb{R}^N$ and the subscript j denotes the index of a specific operating condition. Then, the aerodynamic parameters x^* can be computed by

$$x^* = \arg\min_x \ \vec{\varepsilon}(x)^\top \vec{\varepsilon}(x) \qquad (18)$$

Python's SciPy minimization routine is used to solve (18). A smart choice of initial guess x_0 must be used to yield a physically realizable x^*; the choice used in this paper is $x_0 = (2\pi, 2, 0, 0.47)$, where the initial guess of $c_{l,1} = 2\pi$, $c_d = 0$ comes from flat plate theory [21], and the initial guess of $c_{l,2} = 2$, $\alpha_0 = 0.47$ comes from averaging airfoil data from [20].

A. Body Lift Sensitivity

To ensure the multirotor frame isn't producing vertical force that could be skewing the parameter fitting, a body lift term is appended to (16)

$$L_{\text{body}} = \frac{1}{2} \rho V_{\text{vehicle}}^2 C_L^{\text{body}}(\beta_{\text{body}} - \pi/2) S_{\text{body}}$$

where S_{body} is the surface area of the multirotor body, $(\beta_{\text{body}} - \pi/2)$ is the angle of attack of the frame (see Fig. 4), and $C_L^{\text{body}}(\cdot)$ has the form (3) with corresponding parameters $c_{l,1}^{\text{body}}, c_{l,2}^{\text{body}}, \alpha^{\text{body}}$. Then, the optimization (18) is recast to

[4]For fixed wing UAVs, the lift produced by the wing must be added to (16) using the form (3) for its lift. The extra parameters for the wing can then be appended to the parameter vector x and cast into the optimization (18).

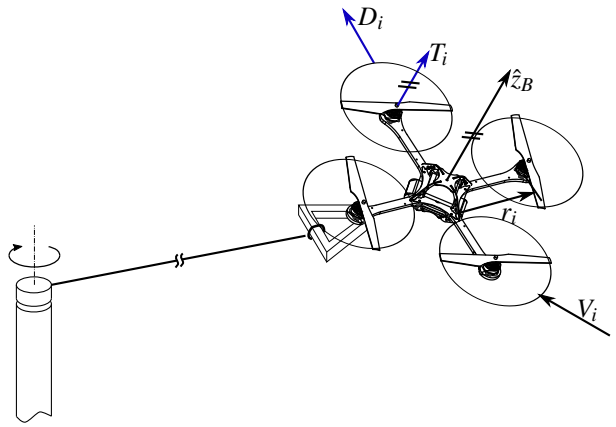

Fig. 5: Tethered quadrotor set-up. In this case, $\hat{z}_i$, $i \in \{1,\ldots,4\}$, are parallel to $\hat{z}_B$.

include this term: first, define the augmented parameter vector $\bar{x} := (x, c_{l,1}^{\text{body}}, c_{l,2}^{\text{body}}, \alpha^{\text{body}})$, the error vector

$$\vec{\bar{\varepsilon}}(\bar{x})_j \;:=\; \vec{\varepsilon}(\bar{x})_j \;+\; L_{\text{body}}(V_{(\text{vehicle},j)}, \beta_{(\text{body},j)}, \bar{x}) \;-\; mg,$$

for $j = 1,\ldots,N$, and thus the optimization becomes $\bar{x}^* = \arg\min_{\bar{x}} \vec{\bar{\varepsilon}}(\bar{x})^\top \vec{\bar{\varepsilon}}(\bar{x})$. This minimization resulted in the optimal $c_{l,1}^{\text{body}}, c_{l,2}^{\text{body}}$ terms to be 0 ($\implies$ $L_{\text{body}} \equiv 0$) indicating that the optimization is insensitive to the body lift term and thus can be excluded from the analysis (16).

IV. EXPERIMENTAL ASSESSMENT

The approach described in Section III is applied to a tethered quadrotor ($n = 4$) as shown in Fig. 5. The tether only provides the centripetal force required for the quadrotor to fly in circles, thereby allowing the quadrotor to achieve very high speeds in a small space [22]. The vehicle is commanded to fly levelled circles (constant height) at various specified constant tangential speeds V_{vehicle}. The control algorithm used is omitted for brevity, but one could use the approach found in [6]. The optimization (18) is performed for $N = 20$ and takes approximately between 2 and 10 hours on a laptop with a third generation Intel-i7 and 8 GB of RAM running Solus Linux and Python 3.5.1. A single call of the thrust/drag/torque map (13)-(15) takes approximately 3 seconds.

Two experiments are done for two different sets of propellers: "soft" propellers[5] made of low rigid plastic meant for low weight and hovering multirotors, and "stiff" propellers[6] made of a carbon composite material and is of high pitch typically meant for forward flying vehicles. The propeller characteristics and corresponding parameters x^* can be found in Table I. The aerodynamic parameters are in the typical range of airfoils [20].

Fig. 6 shows the various rotor forces both using the standard hover approximation (rotor thrust $\propto \Omega^2$, rotor drag $\equiv 0$, rotor torque $\propto \Omega^2$) and using the post-fitted maps (13)-(15).

From the first plot, the collective thrust using the stiff propeller is more than that produced by the soft ones since the vehicles weight is larger. The first principles based model and hover model diverge when the vehicle flies at 7 (for soft) to 9 (for stiff) m/s. The rotor drag is about an order of magnitude lower than the rotor thrust, but becomes significant due to its linear relationship with vehicle speed. The only ground truth available is that the vertical forces must balance, i.e. $\varepsilon(x^*)_j$ should be 0 for all j (all steady state operating conditions). Between 4 and 7 m/s, the hover model for both propellers underestimate the vertical force due to the unmodelled rotor drag, and above this range it overestimates the vertical force.

TABLE I: Propeller characteristics

		Soft[5]	Stiff[6]	APC[7]
Geometry	R	10 cm	10 cm	10 cm
	N_b	2	2	2
	$\max_{y\in[0,R]} \theta(y)$	36 deg	41 deg	45 deg
	$\min_{y\in[0,R]} \theta(y)$	6 deg	14 deg	17 deg
	$\max_{y\in[0,R]} c(y)$	23 mm	23 mm	24 mm
	$\min_{y\in[0,R]} c(y)$	14 mm	6 mm	5 mm
x^*	$c_{l,1}$	6.9	4.2	5.3
	$c_{l,2}$	2.0	2.0	1.7
	c_d	3.7	1.3	1.8
	α_0	20.4 deg	27.5 deg	20.6

A. Model comparison with wind tunnel experiments

In order to reason the grey-box model derived in Section II does indeed capture the true rotor forces, a single propeller + motor is placed in a wind-tunnel at the Institute of Fluid Dynamics (IFD) at ETH Zurich (Fig. 8); direct load measurements are taken at various operating conditions in V, Ω, β. The results can be found in Fig. 7 for an APC high-pitch propeller[7]; the corresponding parameters used in the model (13)-(15) can be found in Table I.

As previously discussed, the hover approximation deteriorates at the higher pitch angles and higher incoming wind speeds (error in thrust is as high as 100 percent). The derived map, however, is able to capture the true load measurements (within, at the worst case, 9 percent) (see Fig. 7).

V. CONCLUSION

A methodology is presented based on a first principles based model and parameter fitting on levelled flight data to predict the aerodynamic forces produced by a rotor in a wide flight regime that includes hover and forward flight. Experiments are done on two different propellers to legitimize the methodology, and the model is further compared with load measurements from wind tunnel experiments on a third propeller. The model developed shows an improvement

[5] Parrot AR.Drone 2.0 propeller
[6] HQP 8x4.5 propeller
[7] APC 8x6 propeller

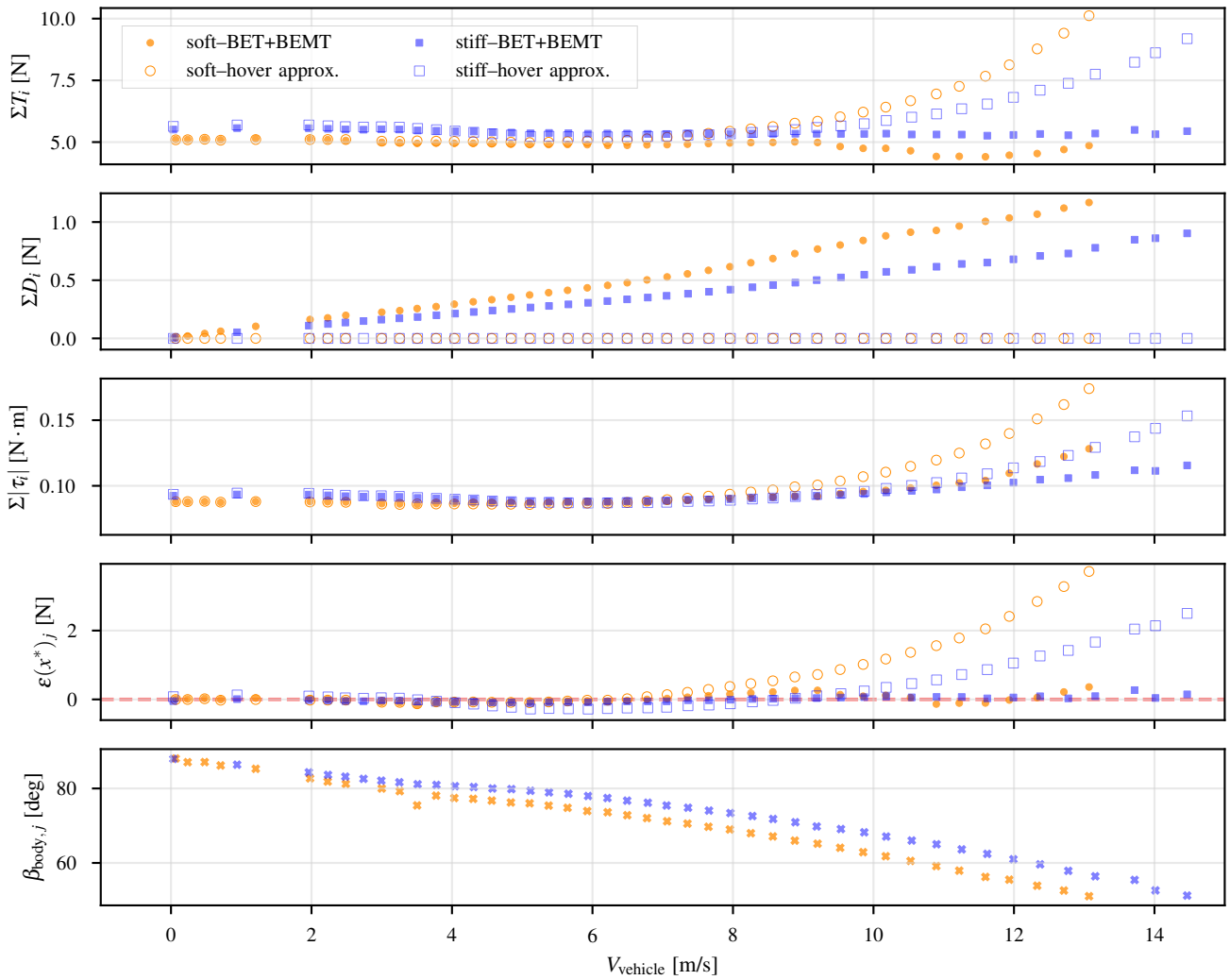

Fig. 6: Rotor forces and torques computed using the post-fitted maps (13)-(15) (labeled BET+BEMT) versus the hover approximation for two types of propellers (Table I). The first plot is the collective rotor thrusts; second is the collective rotor drags; third is the sum of the absolute torques of the rotors (for reference); the fourth plot shows the error (17) in the net vertical force which ideally should be zero (the ground truth, shown in red); the fifth plot shows the associated pitch angles the quadrotor flew in to fly leveled at the corresponding V (for reference).

over the hover model typically used in literature when flying at high speeds.

The rotor thrust and drag maps developed in this paper can be used for the design and control of UAVs, especially for high speed flight. Since the computation time is in the order of seconds, a look-up-table can be used for real-time purposes; using a more accurate thrust and drag model can improve performance of UAVs at these high speeds. Furthermore, the maps can aid in identifying the entire dynamic model of a UAV.

ACKNOWLEDGMENT

This work is supported by and builds upon prior contributions by numerous collaborators in the Flying Machine Arena project. A list of past and present participants of the project is available at http://flyingmachinearena.org/people/.

The authors would also like to thank Andreas Mueller and Professor Thomas Roesgen at the IFD, ETH Zurich.

REFERENCES

[1] M. Y. Amir and V. Abbass, "Modeling of quadrotor helicopter dynamics," in *International Conference on Smart Manufacturing Application*, 2008, pp. 100–105.

[2] D. Mellinger, N. Michael, and V. Kumar, "Trajectory generation and control for precise aggressive maneuvers with quadrotors," *The International Journal of Robotics Research*, vol. 31, no. 5, pp. 664–674, 2012.

[3] S. Bouabdallah, "Design and control of quadrotors with application to autonomous flying," Ph.D. dissertation, Ecole Polytechnique Federale de Lausanne, 2007.

[4] J. Wang, T. Bierling, M. Achtelik, L. Hocht, F. Holzapfel, W. Zhao, and G. Hiong, "Attitude free position control of a quadcopter using dynamic inversion," *AIAA Infotech@ Aerospace*, pp. 29–31, 2011.

[5] T. Luukkonen, "Modelling and control of quadcopter," *Independent research project in applied mathematics, Espoo*, 2011.

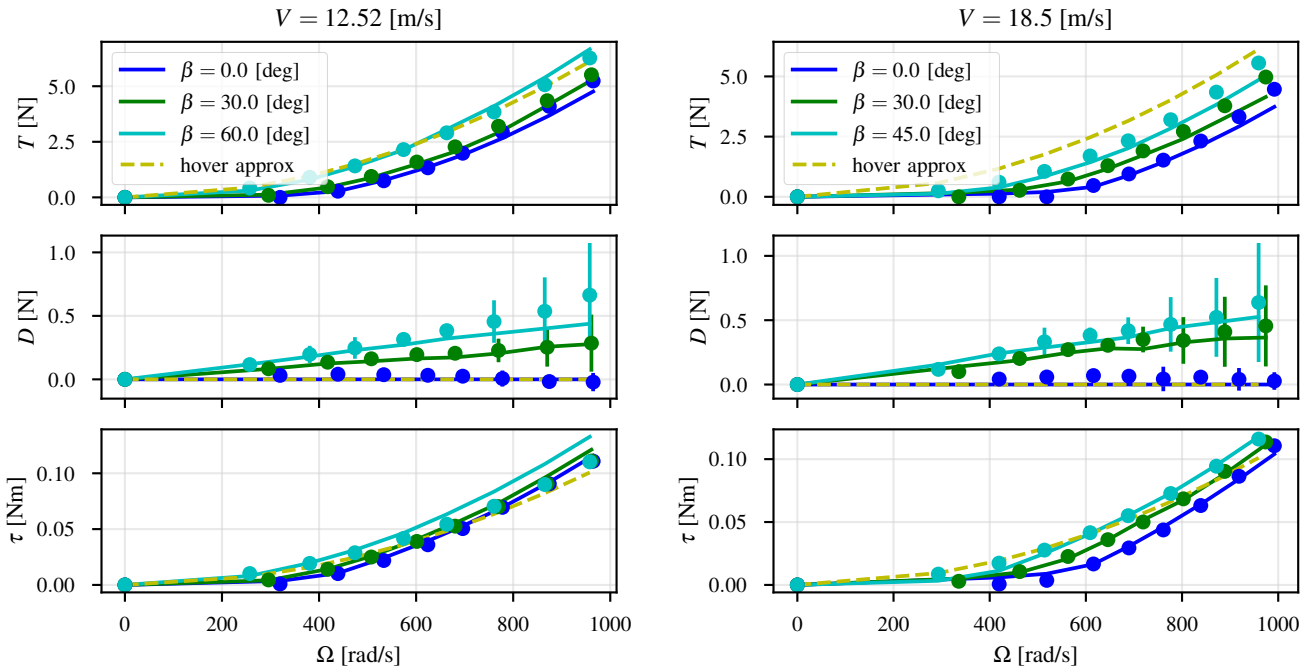

Fig. 7: Wind tunnel measurements (blobs) and predicted loads by the maps (13)-(15) (solid lines) using an APC propeller[7] (Table I). The hover approximation ($T \propto \Omega^2$, $D \equiv 0$, $\tau \propto \Omega^2$) is also shown. The error bars represent one standard deviation.

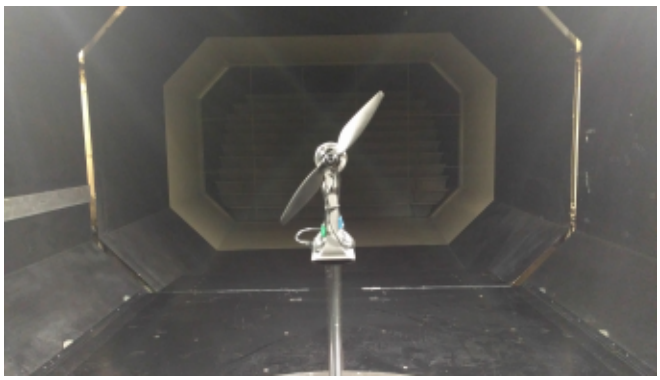

Fig. 8: Wind tunnel and propeller set-up. In this view, wind is going into the page; in this configuration, $\beta = 0$ deg. Different β values are tested by rotating the entire setup about the vertical axis. The load measuring device is an ATI Mini-40 sensor.

[6] M. Schulz, F. Augugliaro, R. Ritz, and R. D'Andrea, "High-speed, steady flight with a quadrocopter in a confined environment using a tether," in *IEEE/RSJ International Conference on Intelligent Robots and Systems*, 2015, pp. 1279–1284.

[7] H. Bouadi, M. Bouchoucha, and M. Tadjine, "Modelling and stabilizing control laws design based on backstepping for an uav type-quadrotor," *IFAC Proceedings Volumes*, vol. 40, no. 15, pp. 245 – 250, 2007.

[8] T. Bresciani, "Modelling, identification and control of a quadrotor helicopter," Master's thesis, Lund University Libraries, 2008.

[9] H. C. T. E. Fernando, A. T. A. D. Silva, M. D. C. D. Zoysa, K. A. D. C. Dilshan, and S. R. Munasinghe, "Modelling, simulation and implementation of a quadrotor uav," in *IEEE 8th International Conference on Industrial and Information Systems*, Dec 2013, pp. 207–212.

[10] A. Koehl, H. Rafaralahy, M. Boutayeb, and B. Martinez, "Aerodynamic modelling and experimental identification of a coaxial-rotor uav," *Journal of Intelligent & Robotic Systems*, vol. 68, no. 1, pp. 53–68, 2012.

[11] G. Hoffmann, H. Huang, S. Waslander, and C. Tomlin, "Quadrotor helicopter flight dynamics and control: Theory and experiment," in *AIAA Guidance, Navigation and Control Conference and Exhibit*, vol. 2, 2007.

[12] R. Bapst, R. Ritz, L. Meier, and M. Pollefeys, "Design and implementation of an unmanned tail-sitter," in *IEEE/RSJ International Conference on Intelligent Robots and Systems*, Sept 2015, pp. 1885–1890.

[13] S. Lupashin, M. Hehn, M. W. Mueller, A. P. Schoellig, M. Sherback, and R. D'Andrea, "A platform for aerial robotics research and demonstration: The flying machine arena," *Mechatronics*, 2014.

[14] M. Orsag and S. Bogdan, *Influence of Forward and Descent Flight on Quadrotor Dynamics*. INTECH Open Access, 2012.

[15] J. Leishman, *Principles of Helicopter Aerodynamics, Second Edition*, ser. Cambridge Aerospace Series. Cambridge University Press, 2006.

[16] W. Khan and M. Nahon, "Toward an accurate physics-based uav thruster model," *IEEE/ASME Transactions on Mechatronics*, vol. 18, no. 4, pp. 1269–1279, Aug 2013.

[17] M. Selig, "Modeling full-envelope aerodynamics of small uavs in realtime," in *AIAA Atmospheric Flight Mechanics Conference*, p. 7635.

[18] E. Kulunk, *Aerodynamics of wind turbines*. INTECH Open Access Publisher, 2011.

[19] R. Shevell, *Fundamentals of flight*. Prentice-Hall, 1983.

[20] R. W. Beard and T. W. McLain, *Small unmanned aircraft : theory and practice*. Princeton, N.J. Princeton University Press, 2012.

[21] D. Darmofal and A. U. Mark Drela, "Introduction to aerodynamics," March 2016.

[22] M. Schulz. High-g quadrocopter training: exploring the limits. Youtube. [Online]. Available: https://youtu.be/iJPy1geXu4M